# PHOTOMASK

BACUS—The international technical group of SPIE dedicated to the advancement of photomask technology.

SPIE Extreme Ultraviolet Lithography

# Simulation of polychromatic effects in high NA EUV lithography

**Andreas Erdmann, Hazem Mesilhy, and Peter Evanschitzky,** Fraunhofer Institute for Integrated Systems and Device Technology (IISB), Schottkystrasse 10, 91058 Erlangen, Germany; **Qais Saadeh and Victor Soltwisch,** Physikalisch-Technische Bundesanstalt (PTB), Germany; **Simon Bihr and Jörg Zimmermann,** Carl Zeiss SMT GmbH, Germany; **Vicky Philipsen,** imec, Leuven, Belgium

## ABSTRACT

State-of-the-art EUV exposure systems utilize EUV radiation around 13.52 nm with a full band spectrum extending from 13.2 nm to 13.8 nm. The variation of the wavelength in this range modifies the diffraction angles with an impact on the image blur and non-telecentricity effects. Dispersion of the materials on the EUV mirrors and on the 3D mask introduces an additional sensitivity of the imaging characteristics to the exposure wavelength. We employed the simulation models of the Fraunhofer IISB lithography simulator Dr.LiTHO in combination with measured optical material data from PTB to quantify the resulting image impact and to differentiate between the identified contributors to polychromatic imaging effects.

## 1. Introduction

EUV sources emit a broad spectrum of light ranging from the soft X-ray to the DUV region of the electromagnetic spectrum. Although the Mo/Si multilayer mirrors select a narrow spectral range (full width half maximum peak of EUV light centered at 13.52 nm) from the source in the EUV region, they reflect light in the DUV (and visible) spectral region as well. The resulting out-of-band (OOB) radiation and resulting lithographic effects[1] are beyond the scope of our investigations of polychromatic effects. Instead, we focus our investigations on the full band (FB) spectrum extending from 13.2 nm to 13.8 nm. Figure 1 presents a typical full band spectrum of a EUV exposure system.

Although the spectral bandwidth of KrF and ArF excimer laser sources is considerably smaller than the bandwidth of EUV light for lithographic exposures, the resulting image blur in DUV lithography has been investigated by several authors[2-4] and is considered in state-of-the-art optical proximity correction (OPC) for DUV lithography.[5] Typical spectra of state-of-the-art EUV light sources and their impact on the imaging performance are discussed in a recent publication of van Kerkhof et al.[6]

We employ basic imaging scenarios to investigate the physical origins and related chromatic effects for high NA EUV lithography. Even a small wavelength variation in the range between 13.2 nm and 13.8 nm has a certain impact on diffraction angles. The performance of the multilayer mirrors in the EUV projection optics and EUV mask blank is strongly wavelength-dependent as well. This affects the characteristics of the projection lens and of the mask. Dispersion of materials in the EUV mirrors and on the 3D mask introduces an additional sensitivity of the imaging characteristics to the exposure wavelength. Wavelength-dependent Jones pupils describe the specific characteristics of the mirrors in the EUV projection lens. The wavelength-dependent refractive index n and extinction coefficient k of the materials on the EUV mask constitutes input parameters for the EUV mask models. The optical material data (n and k) for the simulations in this deliverable were measured by PTB.
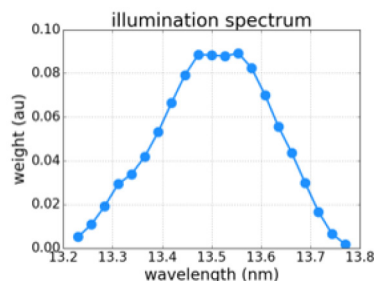
Figure 1. Typical full band spectrum of a EUV exposure system.

SPIE.

11854-05

# EDITORIAL

## The Relentless Pursuit of Perfection

**Glen Scheid,** Micron Technology, Inc., Mask Technology Center

Remember the Lexus slogan when Toyota first brought the brand to market in 1989? Their slogan was "the relentless pursuit of perfection." It defined quality without even using the word. Toyota is legendary when it comes to quality, and their great branding extended deep into their manufacturing culture. Today, technology has become the biggest selling point of modern cars. I may be biased, but I think that, within the technology sector, the photomask industry is the most relentless in our pursuit of product perfection. Consistently held to the highest standards, photomasks are reaching angstrom-level precision while continuing to be produced at a competitive cost and turn time with extremely low reject rates.

This month marks my 20th year as a mask maker. If you asked me what I thought photomask quality was all about when I started, I would have probably said something along the lines of "our ability to consistently meet the spec." Today, however, I look at the photomask and see quality more broadly as the intersection of company culture and industry technology. It is the constant reach for perfection while incorporating the best new tools and manufacturing techniques. While it may seem impossible to have a physical photomask exactly match a computer-drawn spec, there have been emerging areas in recent years that have made me start looking at this as something that we can get seriously close to within the next couple of decades.

One blossoming opportunity with the introduction of EUV masks is the increased culture of collaboration between users and makers. Because EUV masks are held to a higher standard in the wafer fabs, we see mask users taking a central role in mask requalification, now done with high frequency at the point of use. EUV wafer fabs will need to engage in mask inspection, wet cleaning, particle removal, and, one day, re-pellicle. As an industry, this brings the opportunity for deeper exchange of best-known methods with mask users.

A second promising area is the intense reinvigoration of capital suppliers on EUV. In addition to the major suppliers introducing new machines, there have also been some new suppliers entering the market with fresh ideas and techniques. Upcoming technologies include EUV pellicle development, phase and reflectance metrology, and mask data prep. With improved metrology precision combined with upcoming technologies like e-beam and actinic pattern inspection, mask makers will see the mask with unprecedented resolution, allowing us to further understand and reduce manufacturing defects and dial in accuracy like never before.

Finally, the software side of mask making, which has been the backbone of factory automation, is beginning to unlock new operational insights to further improve manufacturing quality. Consider improved analytics through data science and the potential of machine learning, expanded use of mask process correction to dial in the last few drops of lithographic and process error, and the multitude of multi-beam effect corrections that increase with each generation of tool. We are in an age of computational manufacturing that could eventually allow us to fully control the size and placement of every individual pixel on the mask.

Coming off extraordinary progression in 193nm mask quality, we are entering EUV at a significantly stronger starting point. If manufacturing perfection is possible, this is the industry that will reach it. I look forward to continuing our relentless pursuit with this amazing BACUS community.
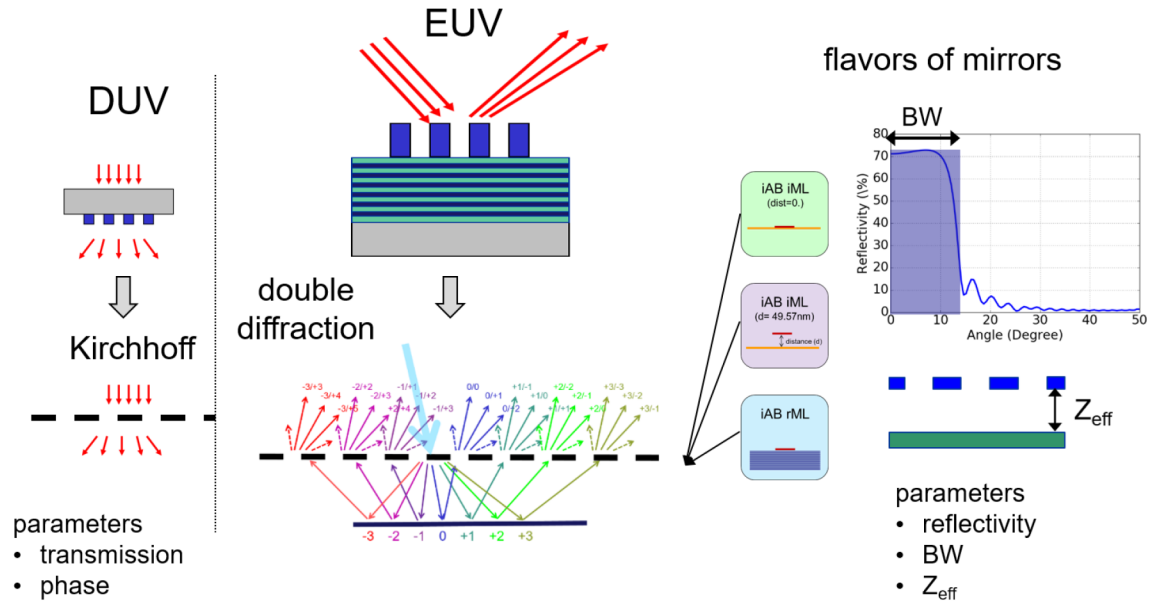
Figure 2. Hybrid mask models of Dr.LiTHO. Left: DUV mask geometry (top) and simplified representation by an infinitely thin absorber (Kirchhoff model, bottom). Center: EUV mask geometry (top) and simplified representation by a double diffraction model (bottom). Right: Different options for the specification of the mirror in the double diffraction model by an idealized mirror (iML) or by a real multilayer (rML). The idealized mirror is described by simulated/measured reflectivity data or by a given bandwidth (BW). The parameter $Z_{eff}$ specifies the distance between the mirror and the ideal infinitely thin absorber (iAB) or a real thick absorber (rAB, not shown in this figure).
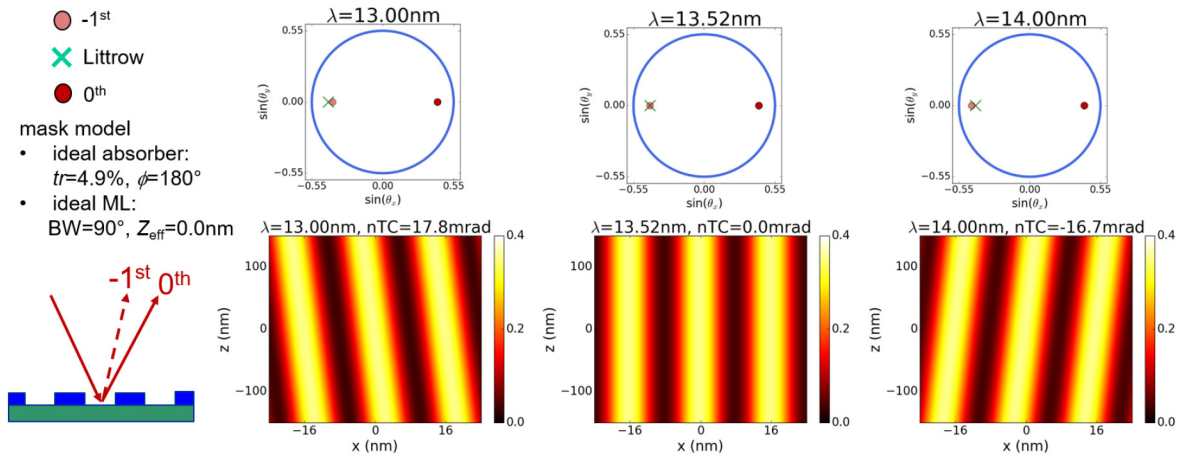


Figure 3. Pupil plots and corresponding aerial images for a single source point illumination at three different wavelengths $\lambda$; 8 nm vertical line-space patterns with a pitch of 16 nm; NA = 0.55; mask model and parameters are given in the left column of the figure.

Physically correct simulation of the lithographic image formation in high NA anamorphic systems with central obscuration combines the modeling of the described phenomena. Selected simulation results of the full system are presented at the end of this paper. In addition to this full system simulation, the hybrid mask models of Dr.LiTHO enable a study of individual contributors to polychromatic effects, e.g., a variation of the wavelength dependency of the mask absorber for a wavelength independent multilayer and projection optics. Simulation studies with these hybrid mask models support an in-depth understanding of EUV imaging and improved definition of system specifications.

Section 2 explains the hybrid mask models of Dr.LiTHO. Subsequently, the imaging of dense line-space patterns in a NA 0.55 EUV system is considered to discuss the impact of the modified diffraction character-istics (Section 3), real multilayer (Section 4), and real absorber (Section 5) on polychromatic effects in EUV imaging. The investigations in Sections 3 - 5 employ illuminations with single-source points or pairs of source points to simplify the discussion of the observed effects. Section 6 applies the developed methods for the modeling of a real use case with typical partial coherent illumination and line-space patterns over a distinct range of pitches. The paper ends with a summary and conclusions.

## 2. Hybrid Mask Models

Figure 2 illustrates the idea of hybrid mask models in Dr.LiTHO. The upper left and upper center of the figure show the basic geometry of masks

**mask model**
- ideal absorber:
  $tr$=4.9%, $\phi$=180°
- ideal ML:
  BW=90°,
  $Z_{eff}$=0.0nm
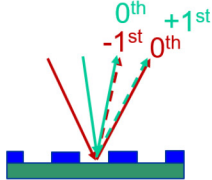
*Figure 4. Aerial images for single-source points (upper and center row) and for pairs of source points (lower row) at three different wavelengths λ. The NILS values are extracted in the nominal image plane at z = 0. All other parameters as given in Figure 3.*



**mask model**
- ideal absorber:
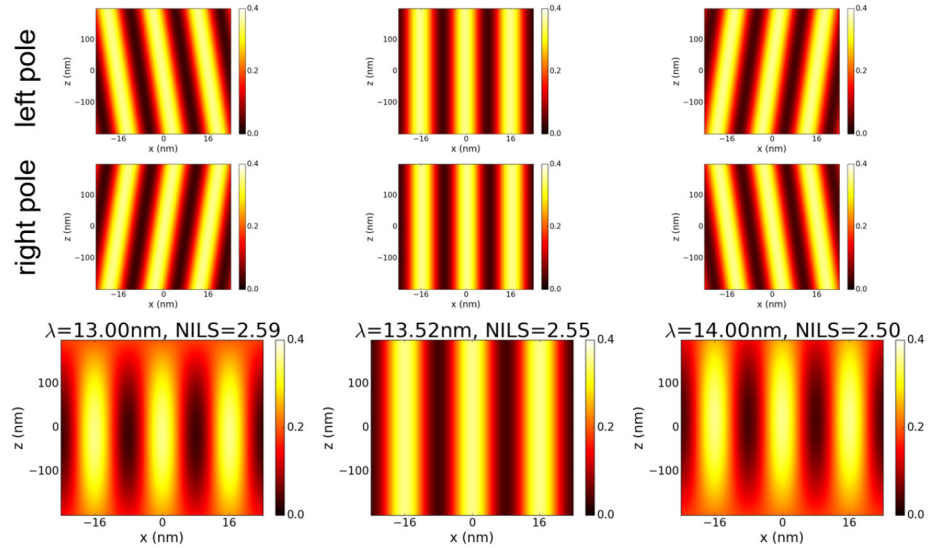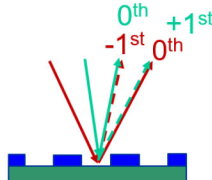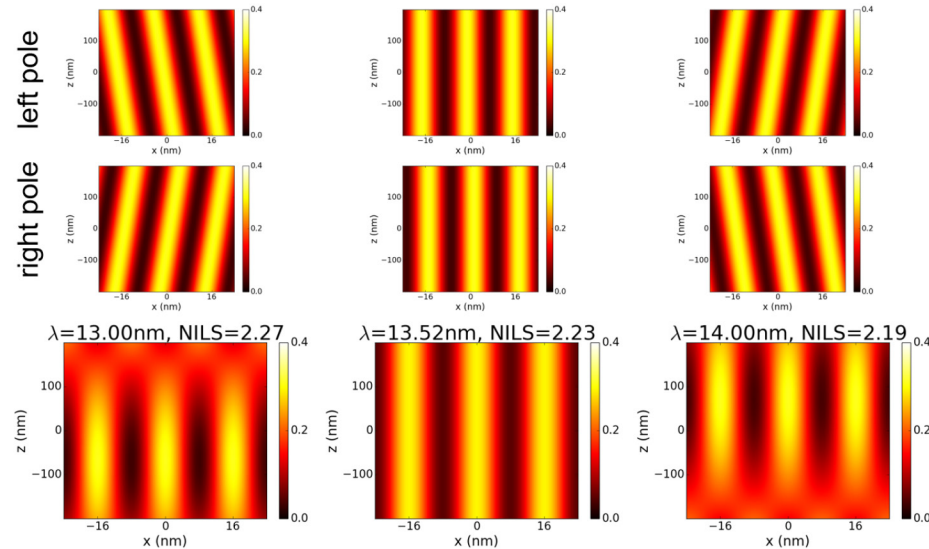  $tr$=4.9%, $\phi$=180°
- ideal ML:
  BW=11°,
  $Z_{eff}$=0.0nm

*Figure 5. Aerial images for single-source points (upper and center row) and for pairs of source points (lower row) at three different wavelengths λ. Bandwidth support of the ideal mirror is limited to BW = 11°. All other parameters as given in Figure 4.*

for DUV and EUV lithography. Incident light from the top of the figure illuminates transmissive DUV masks through a transparent substrate (gray box). The diffracted light from the absorber pattern (blue rectangles) propagates towards the projection lens (not shown in the figure). In a simplified scheme (Kirchhoff model) an infinitely thin absorber with a distinct transmission and phase approaches the mask geometry.

Reflective masks for EUV employ a Bragg-type multilayer mirror (blue and green horizontal stripes) on top of the substrate to reflect the incident light. A double diffraction model is used to analyze the imaging characteristics of the EUV mask. It separates the mask into an absorber and a mirror. Both the absorber and the mirror can be described by real 3D geometries, e.g., absorber/multilayer with given thickness values, or by idealized objects, e.g., infinitely thin absorber with a given transmission and phase, or a mirror with a distinct reflectivity and phase of the

reflected light. As indicated in the right part of the figure, the mirror is specified by simulated/measured reflectivity data versus incident angle or by a given bandwidth (BW) or ranges of incident angles where the light is reflected with a constant (non-zero) reflectivity. To emulate the partial penetration of the light in a real multilayer, an effective mirror distance $Z_{eff}$ is introduced as an additional parameter of the model.

The hybrid mask models of Dr.LiTHO are implemented by complex transfer matrices (T-boxes). The parameters for the computation of these transfer matrices depend on the chosen model option for the absorber and mirror, respectively. The individual transfer matrices are combined in a system matrix that enables the computation of complex diffraction efficiencies of all diffraction orders for a given incidence or illumination direction (see reference[7] for details). The implementation of the hybrid models provides the option to vary (wavelength-dependent)
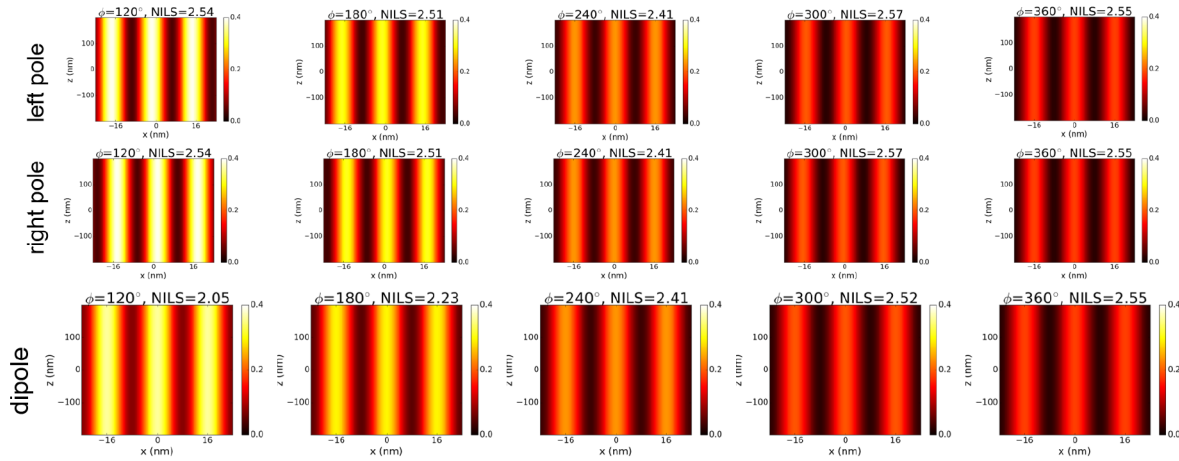
*Figure 6. Aerial images for single-source points (upper and center row) and for pairs of source points (lower row) versus phase ϕ of the transmitted light through an infinitely thin absorber. Bandwidth support of the ideal mirror is limited to BW = 11°. All other parameters as given in Figure 4.*
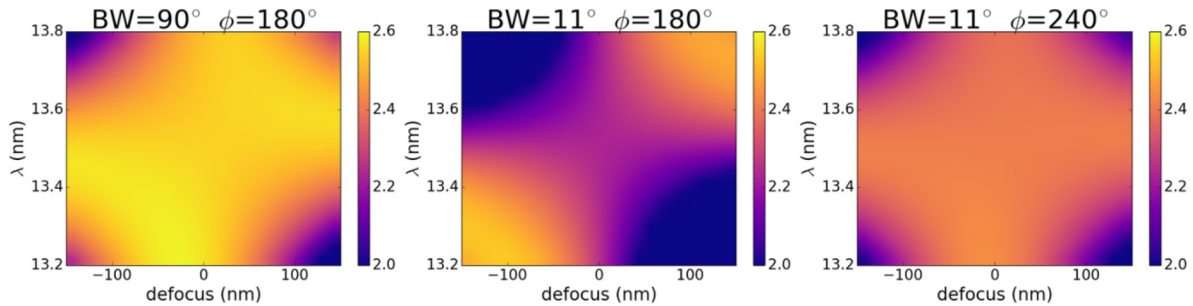


*Figure 7. Simulated NILS of a EUV mask with a thin absorber (tr = 4.9%) and idealized multilayer with a reflectivity of 70% and $Z_{eff}$ = 0 nm and three different combinations of multilayer angular support (BW) and phase of the transmitted light. All other parameters as given in Figure 4.*

parameters of individual components of the mask and imaging system independently from related effects, e.g., wavelength-dependent effects, in other parts of the lithographic system. These unique features of the Dr.LiTHO hybrid mask models are applied in the following sections to characterize the individual contributors to 3D mask (M3D) and polychromatic effects in high NA EUV imaging systems.

## 3. Modified Diffraction Characteristics of Idealized Absorber and Multilayer

The impact of the diffraction characteristics of an idealized absorber and multilayer is investigated for the imaging of vertical (y-parallel) line-space patterns with a pitch p of 16 nm and 1:1 duty ratio between lines and spaces with a NA 0.55 anamorphic system. We consider individual unpolarized source points or pairs of source points with a fixed position in the illumination pupil that support a symmetric two-beam interference scenario for a monochromatic exposure wavelength λ of 13.52 nm. The position of the source points in this so-called telecentric illumination or Littrow mounting is given by σ = λ / (2 p NA); see also upper row of Figure 3. An infinitely thin absorber with a double pass transmission tr of 4.9% and a (wavelength-independent) phase shift ϕ of 180° and an ideal mirror with a constant reflectivity of 70% for all incidence angles (BW = 90°) at zero distance from the absorber ($Z_{eff}$ = 0 nm) are used. The specific transmission and phase values of the absorber are chosen because they provide 100% contrast for an equivalent DUV imaging scenario.

### 3.1 Non-telecentricity effects for single pole imaging versus wavelength

Figure 3 presents pupil plots and corresponding aerial images for a single source point illumination at three different wavelengths. The used symbols for the marking of positions in the pupil plots, the parameters and principle sketch of the mask model are given in the left column. The top row shows pupil plots with positions of the 0th and -1st diffraction order and of the Littrow mounting (perfect symmetric position of the two diffraction orders inside the pupil). Interference of the two diffraction orders emerging from the exit pupil of the scanner optics generates the aerial image in the lower row. The position z = 0 nm specifies the nominal image plane. The variation of the image over a focus range from -150+nm to +150 nm is presented.

For the nominal wavelength of 13.52 nm the position of the -1st order exactly coincides with the Littrow mounting. The resulting interference pattern is parallel to the z-axis. The CD and feature position are independent of focus (z-axis), suggesting an infinite depth of focus (DoF) and zero non-telecentricity (nTC).

The situation changes for other wavelengths. The variation of the diffraction angle versus the wavelength shifts the position of the -1st order to the left or right of the Littrow mount. The asymmetric position of the diffraction angles in the exit pupil produces a tilted interference pattern and nTC values of 17.8 mrad and -16.7 mrad, respectively. The image CD is constant along with the focus or z-axis. Real systems employ a certain spectrum of wavelengths and partial coherence. The non-telecentricity effects for dense line-space patterns in such a system are significantly lower.
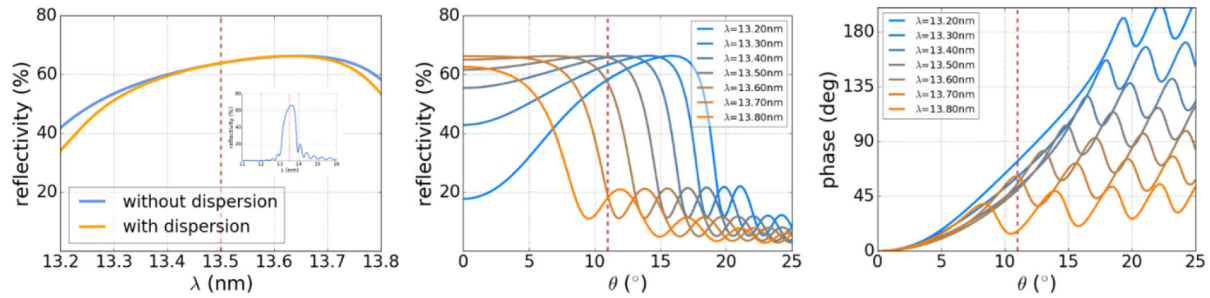
# GREUS
## N • E • W • S



Figure 8. Simulated reflectivity data of a typical Mo/Si multilayer stack without intermixing. Left: Reflectivity versus wavelength λ at θ = 5.4°. The small figure inset presents computed reflectivity data over a larger wavelength range (without material dispersion). Center: reflectivity versus incident angle θ . Right: phase of reflected light versus incident angle θ .
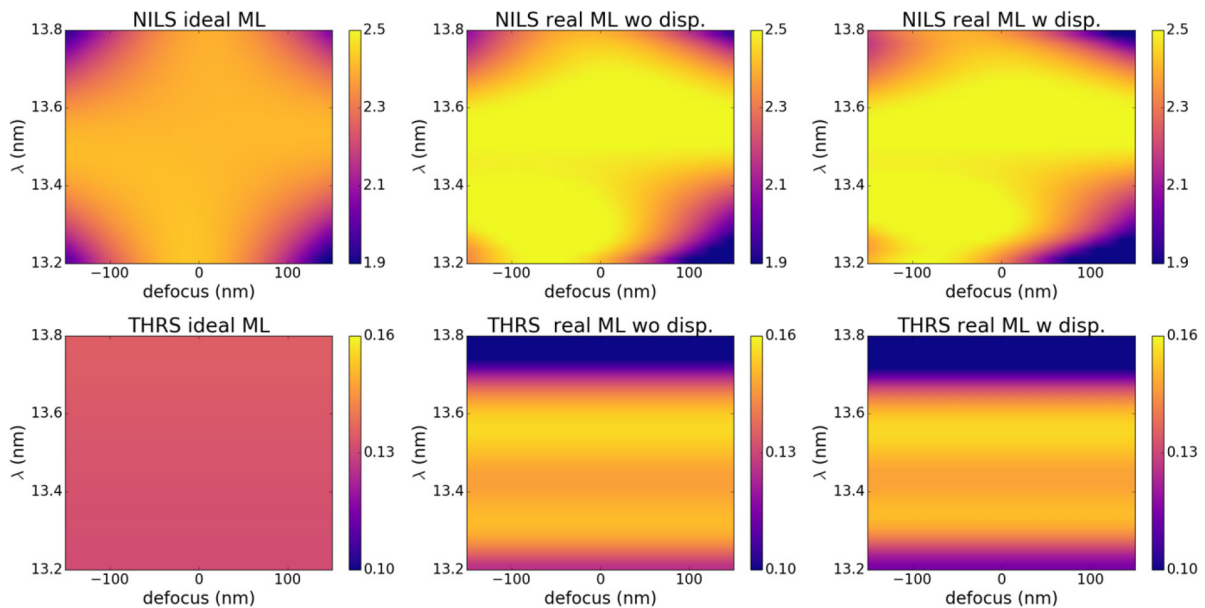


Figure 9. Simulated NILS (upper row) and THRS (threshold-to-size, lower row) of a EUV mask with a thin absorber (tr = 4.9%, ϕ = 240°) for different multilayer options. Left idealized multilayer (BW = 11°, $Z_{eff}$ = 50 nm), center: real Mo/Si multilayer without material dispersion, right: real Mo/Si multilayer without material dispersion. All other parameters as given in Figure 4.

## 3.2 Image-blur effects for double pole imaging versus wavelength

Next, we investigate the imaging of the dense line-space pattern with two symmetrically placed source points. The basic setup, parameters, and resulting images are shown in Figure 4. The same mask model as in Section 3.1 is used. The principle setup on the left of the figure indicates that the role of the $0^{th}$ and the $\pm 1^{st}$ diffraction order interchanges between the left and right poles. The aerial images obtained with the left pole in the upper row of Figure 4 are identical to the single-pole images from Figure 3. The right pole images in the second row are flipped versions of the left pole images. The (incoherently) superposed left and right pole images in the lower row indicate a significant image blur and contrast loss mechanism. The image blur increases with the deviation from the nominal wavelength and with the distance from the nominal image plane at z = 0.

The observed contrast loss results from the opposite image shift of the left/right pole images at out-of-focus conditions. A closer look at the aerial images in Figure 4 reveals that the image blur is not (exactly) symmetric to the nominal image plane at z = 0. The best focus (BF) of images for the larger wavelength is shifted towards positive z-values,

i.e., in the direction of the projection lens. The BF of images for the smaller wavelength is shifted in the opposite direction. Such BF shifts versus wavelength indicate a small chromatic aberration of the system.

Notably, the reported NILS values are below a theoretical value of π for a corresponding DUV system with an infinitely thin mask with a transmission tr = 4.9% and phase ϕ = 180°. This observed contrast loss results from the use of unpolarized light and double diffraction. Only a certain part of the downward diffracted light illuminates the absorber in the upward direction (after reflection from the multilayer mirror). The diffraction losses increase with decreasing pitch. It is important to note that the phase and transmission values of the thin mask are given for a double pass (downward + upward). A 90° phase shift introduces a phase asymmetry of the diffracted light and image shifts. An identical illumination from the top and bottom of the absorber would compensate for the image shift. However, the different illumination from the top and bottom of the absorber causes a non-vanishing image shift.

The diffraction losses (and resulting image asymmetries) become even more pronounced when the angular support or BW of the ideal multilayer is reduced. Figure 5 exhibits simulation results for a perfect mirror

**BACUS**
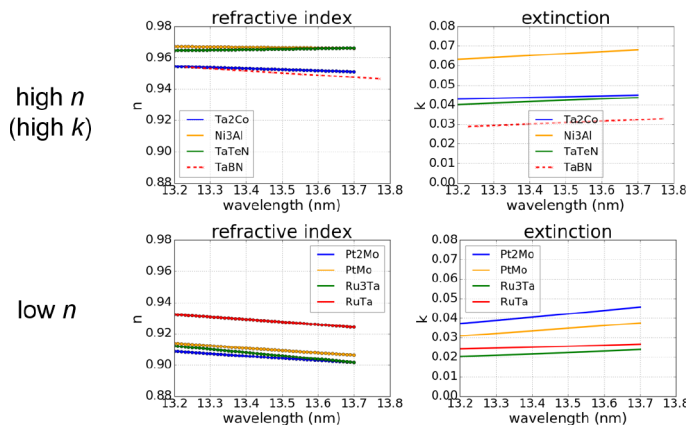
high *n*
(high *k*)

low *n*

Figure 10. Material dispersion data (refractive index n and extinction coefficient k) of investigated absorber materials in the full band (FB) spectral range (measured by PTB).
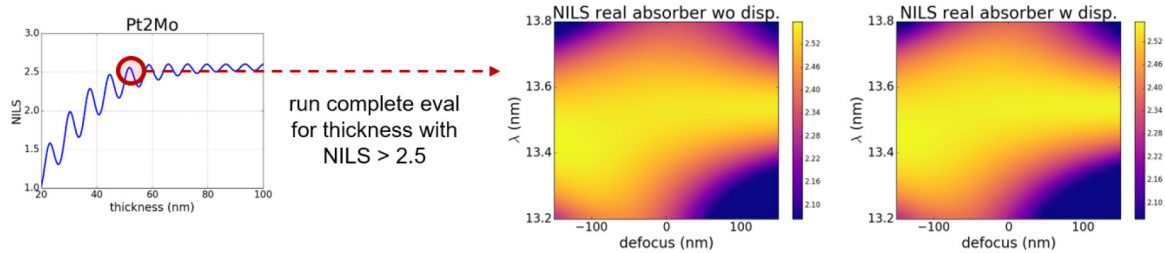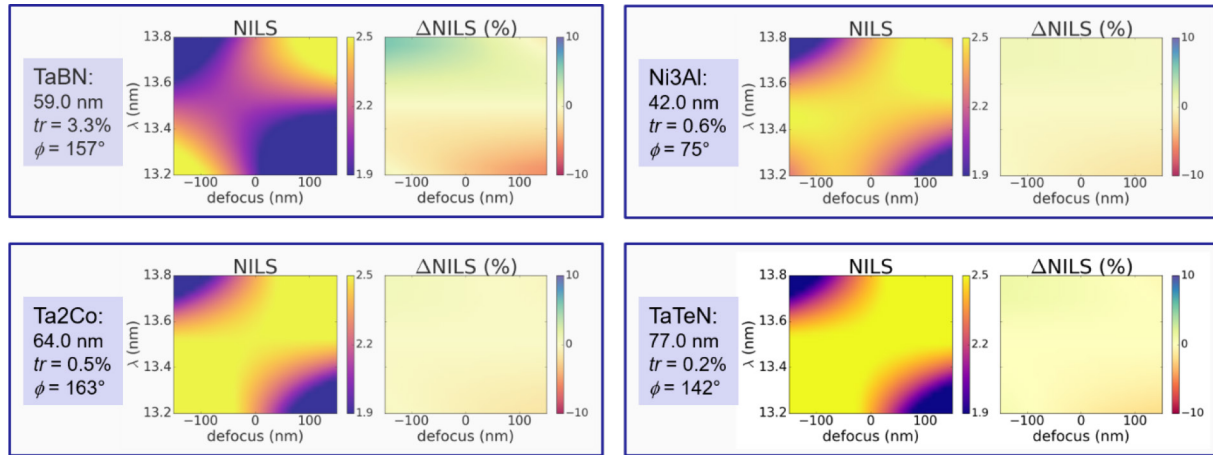
Figure 11. Simulation procedure for evaluation of 3D absorbers.

Figure 12. Simulated NILS for different high n absorber materials for an idealized multilayer mirror with BW = 11° and $Z_{eff}$ = 50 nm. Each panel exhibits the used absorber, the NILS with consideration of material dispersion, and the difference of the NILS values with and without dispersion. All other parameters as given in Figure 4.



Figure 13. Simulated NILS for different low n absorber materials for an idealized multilayer mirror with BW = 11° and $Z_{eff}$ = 50 nm. Each panel exhibits the used absorber, the NILS with consideration of material dispersion, and the difference of the NILS values with and without dispersion. All other parameters as given in Figure 4.
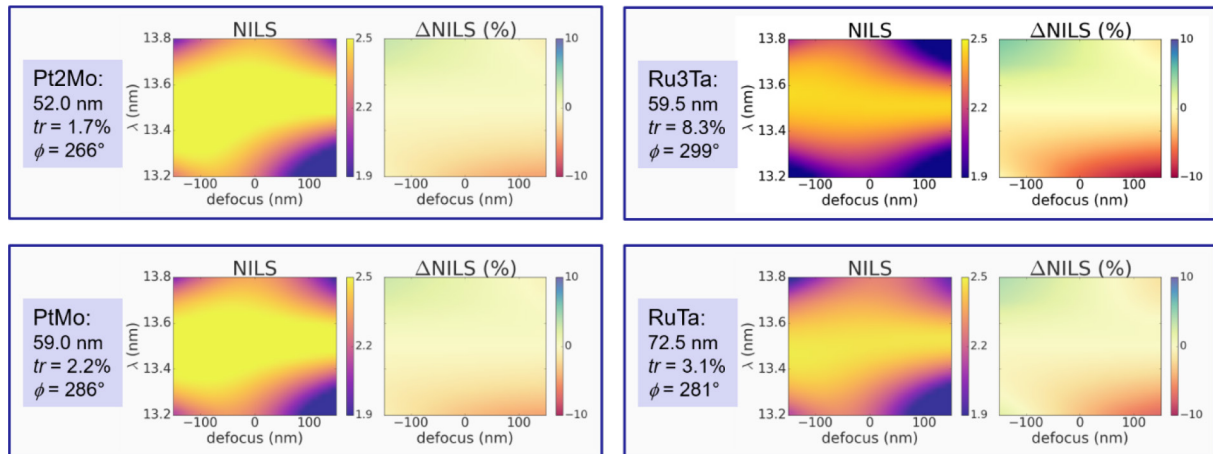
with BW = 11° (similar to the reflectivity support of a real multilayer). Obviously, the missing contribution of reflected light from the mirror reduces the intensity of the resulting images. The images are created by fewer orders of back-reflected light and exhibit more pronounces asymmetries. The shifts of the best focus position at 13.0 nm and 14.0 nm become more pronounced than the focus shifts for the mirror with full bandwidth support (BW = 90°). The image shift for the individual poles and for λ = 13.52 nm increases as well (see top and center row of the second column from the right in Figure 5). Incoherent superposition of the oppositely shifted images causes image blur and a further drop in the NILS values.

The observed phenomena, i.e., increased image blur at the center wavelength and increased shift of the best focus position at the lower and upper limits of the full band spectrum occur for idealized multilayer mirrors at larger distances ($Z_{eff}$ = 50 nm) and for real multilayers as well.

### 3.3 Image-blur effects versus absorber phase

The transversal (x) and longitudinal (z, focus) symmetry of an image obtained with an attenuated phase shift mask (attPSM) can be tuned by the phase φ of the transmitted light through the mask. Figure 6 presents simulation results for the considered imaging scenario and varying phases φ of the mask. The values of φ referring to a double pass through the infinitely thin absorber.

A larger phase shift and corresponding destructive interference of the diffracted light in the forwarding direction (downward propagation $0^{th}$ diffraction order) reduces the brightness of the image. A significant part of the light is diffracted to higher orders at larger diffraction angles and is not reflected back by the bandwidth-limited mirror. On the other hand, the shift between the images (as obtained by the individual poles) is reduced. The contrast of the dipole images increases for larger amounts of phase shifts. A phase shift φ ≈ 240° provides the best tradeoff to get high NILS and high image intensity or threshold-to-size. Similar optimum phase shifts for EUV attPSM were reported in several previous simulation studies.[8, 9] These studies attributed their observations to M3D effects. The results of our simulations demonstrated for the first time that the peculiarities of the phase of attPSM for EUV can be explained by a 2D mask model with an infinitely thin absorber and a simplified multilayer mirror. Of course, 3D mask effects, especially the waveguide phenomena in EUV mask[10] contribute to the imaging behavior of EUV masks as well. Selected effects are discussed in Section 5.
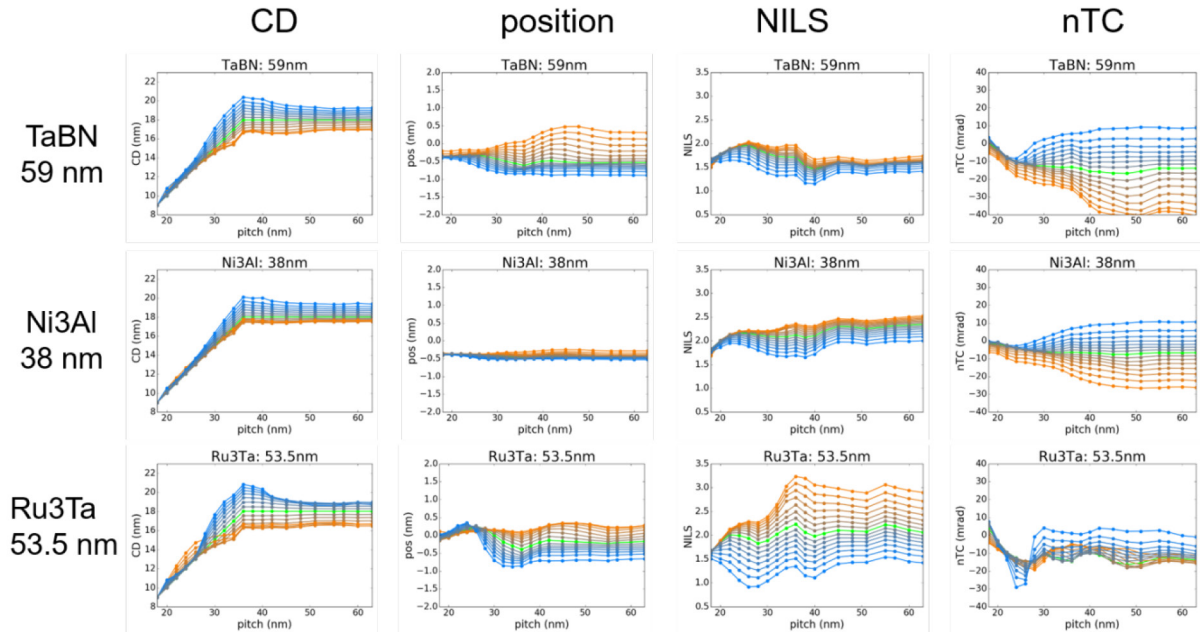
Figure 14. Spectral dependency of lithographic performance of vertical line-space pattern versus pitch for three typical absorber materials. The wavelength ranges from 13.3 nm (blue) to 13.8 nm (orange), and green curves - center wavelength of 13.52 nm.

Figure 7 summarizes the observations of Section 3 by plotting the NILS versus wavelength λ and defocus on three different cases. The left part of the plot suggests relatively high NILS values for an idealized multilayer mirror that reflects light over the complete range of incidence angles (BW = 90°). The limitation of the angular range of high reflectivity to BW = 11°, i.e., a more realistic case, results in a significant drop of the NILS at the center wavelength and in the nominal image plane of the system (defocus = 0 nm). Increasing the amount of the phase shift of the transmitted light of the thin absorber to 240° recovers a large part of the NILS.

## 4. Effects of Real Multilayer

The reflectivity of multilayer mirrors for EUV is strongly wavelength-dependent. The Bragg-type mirrors for the projection optics and mask substrate consist of 40 bilayers of Mo and Si with an approximate thickness $d \approx \lambda / (2 \cos \theta)$ with typical incident angles θ close to the chief ray angle at an object (CRAO). Dispersion of the materials in the multilayer stack affects the reflectivity of the multilayer as well. The multilayer parameters are tuned to provide a high reflectivity over distinct ranges of wavelengths and incident angles.

The left part of Figure 8 shows simulated reflectivity data versus wavelength for an incident angle θ of 5.4° (approximate value of CRAO of NA 0.55 system). The simulations are done for a simple Mo/Si multilayer of 40 bilayers (4.0 nm Si and 3.0 nm Mo) without intermixing. The data of the blue curve are computed for a constant refractive index over the complete range of incident angles. The more correct orange curve includes the material dispersion of Mo and Si over the given range of wavelengths. The dispersion impact on the re in the in-band (IB) wavelength range (λ = 13.52 nm ± 1%) is very small. It advances up to a few percent at the limits of the full band spectrum.

The plots at the center and right of Figure 8 present the simulated reflectivity and phase of the reflected light versus the incident angle θ. These data are computed for distinct wavelengths and include the material dispersion. The high reflectivity support of the multilayer for smaller wavelength shifts towards larger incidence angles. Less short-wavelength light is reflected at small incidence angles. The phase of the reflected light at small incidence angles exhibits only a weak depen-

dence on the wavelength.

Figure 9 presents the simulated impact of the multilayer effects on the NILS for a thin absorber with the transmission of 4.9% and an (optimized) phase of 240°. The ideal ML with a wavelength-independent reflectivity support on the left of the figure exhibits constant threshold-to-size (THRS) and NILS values above 2.4 over a large range of wavelengths and defocus values.

The slightly larger bandwidth of the real multilayer and sidelobes in the reflectivity curve of real multilayers help to push the NILS and the threshold-to-size values even to slightly higher values. However, the THRS drops for wavelengths above 13.65 nm and below 13.25 nm. The comparison of the center and right plots indicates a small impact of the dispersion of the multilayer materials on the imaging characteristics.

## 5. Effects of Real Absorber

Finally, we investigate the impact of the 3D absorber and its material properties on the considered imaging example. To exclude the wavelength-dependent impact of the multilayer, an idealized multilayer with BW = 11° and $Z_{eff}$ = 50 nm is used. Figure 10 presents the measured dispersion data for two groups of materials. The top row exhibits the data of TaBN (reference material) and several other alloys with refractive index n > 0.94. Aside from TaBN, these materials are high extinction (k) absorber candidates. The low n materials in the lower row provide candidates for attPSM materials.

The imaging performance of real absorber materials depends strongly on the thickness of the absorber. The 59-nm-thick TaBN reference absorber represents a presently used absorber stack. The thickness of the other used absorbers was determined from the computation of the NILS versus thickness for the nominal wavelength λ = 13.52 and at zero defocus. It was chosen from the first local maximum of the NILS vs. thickness curve above 2.5 (see example for Pt2Mo in Figure 11). Afterwards the NILS values with and without material dispersion were computed versus the FB wavelength range and the focus range between -150 nm and +150 nm.

Figure 12 presents simulation results for the material with high n (high k). Each panel exhibits the absorber material, the chosen thickness and the corresponding transmission and phase according to standard thin
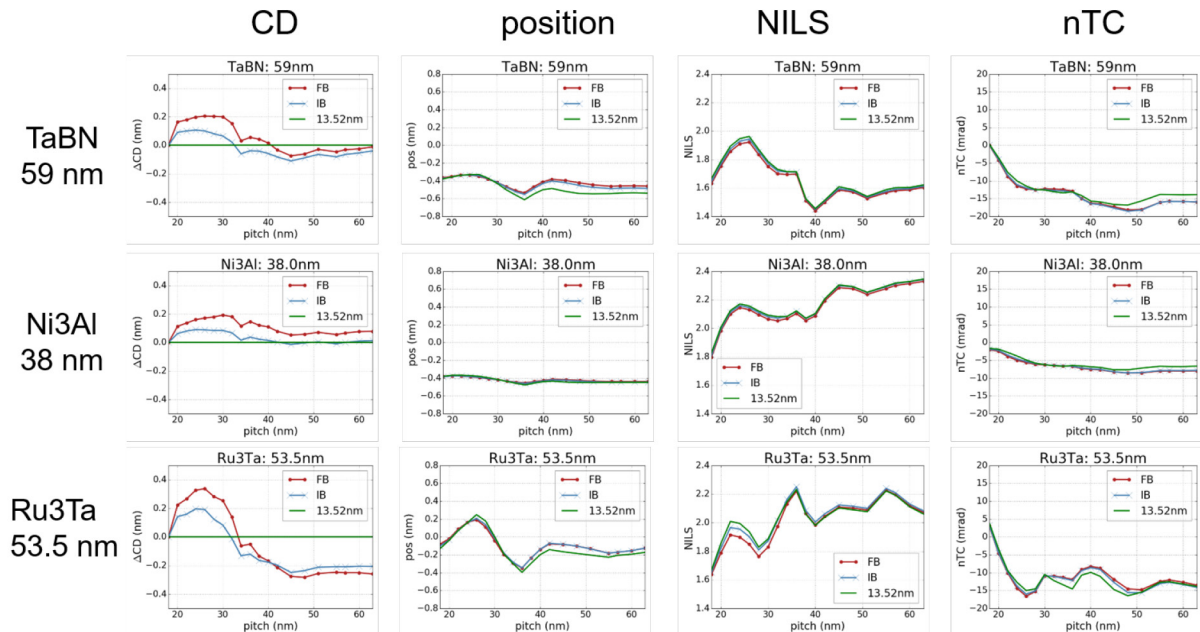
*Figure 15. Spectral dependency of lithographic performance of vertical line-space pattern versus pitch for three typical absorber materials: Monochromatic results (13.52 nm) compared to a full band (FB) and in-band (IB) performance. The value of ΔCD refers to the target CD, i.e., it is zero at 13.52 nm wavelength where the OPC was done.*

film considerations. The NILS data are plotted for the absorber including material dispersion. The values of ΔNILS refer to the difference between the NILS values with material dispersion and the material without dispersion. They indicate the sensitivity of the extracted NILS to material dispersion.

The NILS of the standard TaBN absorbers at the nominal wavelength and defocus drops to about 2.0. As discussed before, this drop of the NILS is caused by the shift of the images that are obtained by the individual poles. Note the similarity between the NILS of the (real 3D) TaBN absorber with a transmission of 3.3% and phase shift of 157° and the idealized absorber with the transmission of 4.9% and a phase shift of 180° in the center of Figure 7.

The transmission values of the other high n (high k) materials in Figure 12 are below 1%. They exhibit less pronounced image shifts between the poles and a significantly lower drop of the NILS at the nominal wavelength and focus position. Alloys with a refractive index above 0.94 require a sufficiently low transmission (below 0.5%) to mitigate image blur at center wavelength and best focus. The dispersion of the absorber material affects the NILS by less than 1%.

Low n absorber materials exhibit a different behavior of NILS versus wavelength and defocus (see Figure 13). The large phase shift in these materials reduces the shift between the images of different poles and provides comfortable NILS values over the complete focus range from -150 nm to +150 nm at the nominal exposure wavelength of 13.52 nm.

The favorable performance of low n material can be attributed to the guiding of light inside the openings of the absorber.[10] This guiding of light helps not only reduce the image shifts. It also helps to transmit more EUV light through these openings and to achieve reasonable values of threshold-to-size (not shown here). On the other hand, the dispersion of low n absorber materials affect the NILS more significantly than high n materials do. It can modify the NILS by several percent over the full wavelength range.

## 6. Impact on Lithography Metrics for Real Use Case

The simulations in this final section combine the diffraction characteristics and the effects of the real multilayer and real absorber for a real use case with partially coherent illumination and through-pitch imaging of a line-space pattern. The simulations are performed for a NA = 0.55 anamorphic system with a center obscuration of 21% (of the full pupil in radius) for an experimentally measured bandwidth spectrum between 13.2 nm and 13.8 nm. The lithographic performance was simulated at several positions in the exposure slit. Here we report only on selected results at the slit edge, which exhibits the most pronounced imaging artifacts. An ideal diffraction limited Jones pupil was assumed for all investigated wavelengths. A Gaussian blur width with a magnitude corresponding to a quarter of the target size was applied to emulate the photoresist effect. Simulations are done for a standard MoSi with intermixing including the dispersion properties of the materials in the multilayer blank. The wavelength-dependent refractive index n and extinction coefficient k of the absorbers are obtained by measurements of PTB (see data in Figure 10).

The considered use cases are vertical lines/spaces versus pitch for a leaf-shaped dipole illumination. First, a simple OPC through pitch was performed to print all features on target for the center wavelength λ = 13.52 nm. The anchor focus and anchor threshold are defined by the largest and smallest pitch, respectively. After that important lithography metrics including CD, position, NILS, and non-telecentricity are computed at other wavelengths (at the recalculated threshold-to-size for the smallest pitch).

The representative simulation results in Figure 14 exhibit the lithographic performance of the presently used TaBN absorber, of Ni3Al as a typical high k absorber, and of RuTa as a low n absorber. Low n absorbers tend to exhibit increased wavelength sensitivity of NILS compared to the other materials. Thin high k materials (Ni3Al) exhibit smaller variations of the feature position versus pitch. Both high k and low n absorbers tend to reduce the non-telecentricity for wavelengths that are different from the center wavelength.

Figure 15 presents simulation results for the same materials and settings when the weighting of the spectral components in the illumination of the mask is included. Three scenarios are investigated. The green curve shows the monochromatic result for the center wavelength of 13.52 nm (identical to the green curve in Figure 14). The blue curves exhibit the in-band (IB) contribution with a wavelength range between $\lambda$ = 13.35 nm and $\lambda$ = 13.63 nm. The red full band (FB) curves present the weighted results of the considered complete wavelength range from 13.2 nm to 13.8 nm.

Both high k ($Ni_3Al$) and low n ($Ru_3Ta$) provide a higher NILS than the reference (TaBN), especially for larger pitches. However, the low n absorber tends to exhibit larger non-telecentricity and variation of CD and feature position versus pitch. These effects can be attributed to the more pronounced phase deformation in these materials.

The weighted superposition of the images for different wavelengths reduces the chromatic impact (of the absorber) on feature size and position. In general, the IB results agree very well with the FB results, which relaxes the required computational effort for the simulation of chromatic effects. Again, low n absorbers exhibit the largest difference between CD values that are obtained from IB and FB computations.

In summary, our investigations indicate that the introduction of new mask absorbers affects the polychromatic imaging characteristics of high NA EUV imaging. For the investigated use cases the weighted effect (over the complete spectrum) on CD and feature positions is below 0.4 nm. Our results suggest that the impact of a potential "wavelength drift" can become more critical for new absorber materials. Low n materials tend to increase chromatic effects compared to high k materials.

## 7. Conclusions

The simulation study of polychromatic and mask topography (M3D) effects in high NA anamorphic systems with central obscuration provided further insights into the operation of EUV masks. The peculiarities of the optimum phase of attenuated PSM for EUV are explained by a combination of double diffraction and ideal (thin) absorber and multilayer. Although the real 3D absorber and multilayer contribute to the specific value of the best absorber thickness and phase as well, the unexpected observation of optimum phase shifts different from 180° can be understood by 2D mask models. This finding corrects previous explanations (of several research groups) of this phenomenon by M3D effects.

The polychromatic simulations confirm that the observed image blur in high NA lithography can be mitigated by two different strategies. Low n absorbers guide the EUV light through the openings in the absorber and create sharper images that are less sensitive to the illumination direction. High n absorbers need to absorb enough light to mitigate image blur. Low n materials are more sensitive to material dispersion than high n. The consideration of real multilayer and material dispersion is important for polychromatic imaging characteristics as well.

## 9. References

1. S. A. George, P. P. Naulleau, C. D. Kemp, P. E. Denham, and S. Rekawa, "Assessing out-of-band effects at the wafer level for EUV lithography," **Proc. SPIE 7636**, pp. 763610-763626, 2010.

2. A. Kroyan, I. Lalovic, and N. R. Farrar, "Effects of 95% integral vs. FWHM bandwidth specifications on lithographic imaging," **Proc. SPIE 4346**, pp. 1244-1253, 2001.

3. T. A. Brunner, D. A. Corliss, S. A. Butt, T. J. Wiltshire, C. P. Ausschnitt, and M. D. Smith, "Laser bandwidth and other sources of focus blur in lithography," *J. Micro/Nanolithogr. MEMS MOEMS* 5(4), pp. 1-7, 2006.

4. P. De Bisschop, I. Lalovic, and F. Trintchouk, "Impact of finite laser bandwidth on the critical dimension of L/S structures," *J. Micro/Nanolithogr. MEMS MOEMS* 7(3), p. 33001, 2008.

5. W. Conley, P. Alagna, S. Hsu, and Q. Zhao, "Impact of bandwidth variation on OPC model accuracy," **Proc. SPIE 9780**, pp. 55 - 64, 2016.

6. M. A. van de Kerkhof, F. Liu, M. Meeuwissen, X. Zhang, M. Bayraktar, R. C. de Kruif, and N. V. Davydova, "High-power EUV lithography: spectral purity and imaging performance," *Journal of Micro/Nanolithography, MEMS, and MOEMS* 19(3), pp. 1-16, 2020.

7. P. Evanschitzky and A. Erdmann, "Advanced EUV mask and imaging modeling," *Journal of Micro/Nanolithography, MEMS, and MOEMS* 16(4), p. 041005, 2017.

8. A. Erdmann, P. Evanschitzky, H. Mesilhy, V. Philipsen, E. Hendrickx, and M. Bauer, "Attenuated phase shift mask for extreme ultraviolet: Can they mitigate three-dimensional mask effects?," *Journal of Micro/Nanolithography, MEMS, and MOEMS* 18(1), p. 011005, 2018.

9. C. van Lare, F. Timmermans, and J. Finders, "Mask absorber optimization: the next phase," *Journal of Micro/Nanolithography, MEMS, and MOEMS* 19(2), p. 024401, 2020.

10. H. M. S. Mesilhy, P. Evanschitzky, G. Bottiglieri, C. van Lare, E. van Setten, and A. Erdmann, "Investigation of waveguide modes in EUV mask absorbers," *Journal of Micro/Nanopatterning, Materials, and Metrology* 20(2), pp. 1 - 18, 2021.

# Industry Briefs

### ■ The First High-Yield, Sub-Penny Plastic Processor

**Samuel K. Moore,** IEEE Spectrum, June 14, 2022

For decades, hopeful techies have been promising a world where absolutely every object will have some kind of smarts thanks to supercheap programmable plastic processors. If you've been wondering why that hasn't happened yet, it's that nobody has built working processors that can be made in the billions for less than a penny each. The problem, according to engineers at the University of Illinois Urbana-Champaign and at British flexible-electronics manufacture PragmatIC Semiconductor, is that even the simplest industry-standard microcontrollers are too complex to make on plastic in bulk.

In research to be presented at the International Symposium on Computer Architecture later this month, the transatlantic team presents a simple yet fully functional plastic processor that could be made at sub-penny prices. The Illinois team designed 4-bit and 8-bit processors specifically to minimize size and maximize the percentage of working integrated circuits produced. Eighty-one percent of the 4-bit version worked, and that's a good enough yield, says team leader Rakesh Kumar, to breach the one-penny barrier.

https://spectrum.ieee.org/plastic-microprocessor#toggle-gdpr

### ■ TSMC Upbeat About Coming Decade

**Monica Chen, Hsinchu, Ines Lin,** DIGITIMES, June 9, 2022

TSMC remains upbeat about its operations in 2022 and the coming decade, while its 3nm process is set to enter volume production later this year, according to company chairman Mark Liu. TSMC has recorded new revenue highs for 12 consecutive years, with its 2021 revenue swelling 24.9% from its 2020 level, Liu said, reiterating its goal of achieving 30% revenue growth in 2022. Its 5nm process (N5) has entered the second year of mass production, buoyed by robust demand for mobile and HPC applications. In 2021, N5 contributed 19% to its total wafer sales, TSMC CEO CC Wei said.

https://www.digitimes.com/news/a20220609PD207/ic-manufacturing-tsmc.html

### ■ Alchip Technologies Offers 3nm ASIC Design Services

**Shannon Davis,** Semiconductor Digest, June 15, 2022

Alchip Technologies announced that its high-performance computing ASIC services are now taking 3nm designs and targeting its first test chip for Q1 2023. The company will unveil its chiplet technology at the TSMC North America Technology Symposium on Thursday, June 16. Alchip becomes the first dedicated high-performance ASIC company to announce total design readiness of their design and production ecosystem. The new service targets TSMC's latest N3E process technology. The company revealed that it completed its design technology and infrastructure during the current quarter and will make available its design methodology within a couple of weeks. Alchip earlier announced to select customers the availability of its 3nm MCM, CoWoS and InFO advanced packaging capabilities and its latest APLink 5.0 (Advanced Package Link) die-to-die IP that is UCIe 1.0 compatible.

https://www.semiconductor-digest.com/alchip-technologies-offers-3nm-asic-design-services/

# Join the premier professional organization for mask makers and mask users!

## About the BACUS Group

Founded in 1980 by a group of chrome blank users wanting a single voice to interact with suppliers, BACUS has grown to become the largest and most widely known forum for the exchange of technical information of interest to photomask and reticle makers. BACUS joined SPIE in January of 1991 to expand the exchange of information with mask makers around the world.

The group sponsors an informative monthly meeting and newsletter, BACUS News. The BACUS annual Photomask Technology Symposium covers photomask technology, photomask processes, lithography, materials and resists, phase shift masks, inspection and repair, metrology, and quality and manufacturing management.

### Individual Membership Benefits include:

- Subscription to BACUS News (monthly)
- Eligibility to hold office on BACUS Steering Committee

**spie.org/bacushome**

### Corporate Membership Benefits include:

- 3-10 Voting Members in the SPIE General Membership, depending on tier level
- Subscription to BACUS News (monthly)
- One online SPIE Journal Subscription
- Listed as a Corporate Member in the BACUS Monthly Newsletter

**spie.org/bacushome**

## CALENDAR

### 2022

**EMLC 2022**
20-23 June
Leuven, Belgium
https://www.emlc-conference.com/

**SPIE Photomask Technology + Extreme Ultraviolet Lithography**
25-29 September 2022
Monterey, California, USA
www.spie.org/puv

### 2023

**SPIE Advanced Lithography + Patterning**
26 February - 2 March 2023
San Jose, California, USA
www.spie.org/al

SPIE, the international society for optics and photonics, brings engineers, scientists, students, and business professionals together to advance light-based science and technology. The Society, founded in 1955, connects and engages with our global constituency through industry-leading conferences and exhibitions; publications of conference proceedings, books, and journals in the SPIE Digital Library; and career-building opportunities. Over the past five years, SPIE has contributed more than $22 million to the international optics community through our advocacy and support, including scholarships, educational resources, travel grants, endowed gifts, and public-policy development. www.spie.org.

**SPIE.**
International Headquarters
P.O. Box 10, Bellingham, WA 98227-0010 USA
Tel: +1 360 676 3290
Fax: +1 360 647 1445
help@spie.org • spie.org

Shipping Address
1000 20th St., Bellingham, WA 98225-6705 USA

**SPIE.EUROPE**
2 Alexandra Gate, Ffordd Pengam, Cardiff,
CF24 2SA, UK
Tel: +44 29 2089 4747
Fax: +44 29 2089 4750
info@spieeurope.org • spieeurope.org

**You are invited to submit events of interest for this calendar. Please send to lindad@spie.org.**